BIMA memo 101 - July 2004

Imaging Simulations with CARMA-23

M. C. H. Wright

Radio Astronomy laboratory, University of California, Berkeley, CA, 94720

ABSTRACT

We simulated imaging for the 23-antenna CARMA telescope in three compact configurations using a model image of Saturn. Simulated *uv* data sampled by the heterogeneous array of 10.4, 6.1, and 3.5 m antennas were used to make mosaic images. Three different Maximum Entropy deconvolutions were used. The best image fidelity was obtained using a joint deconvolution of the interferometer and single dish data. Using the single dish data as a default image, provides a total flux estimate and low spatial frequencies unsampled by the interferometric mosaic. Both methods give higher image fidelity than just using the interferometer data with a total flux estimate. We analyze two problems: i) sampling the short spatial frequencies, ii) Nyquist sampling the large scale structure, and show that the image fidelity is improved by a higher *uv* sampling density. Using the interferometer spacings between 3.5 and 6.1 m sampled by the 3.5 m antennas further improves the image fidelity because the interferometer observations provide better quality data for these short spatial frequencies, than can be obtained from the joint deconvolution with the 10.4 m single dish data.

1. Introduction

Many astronomical studies require observations of images over a wide range of spatial scales. A 10 m antenna at a wavelength of λ 1.3 mm has a field of view of $\sim 30''$; sources larger than this require a mosaic of interferometer and single dish observations at multiple pointing centers. The case for a homogeneous array has been well studied (e.g. Cornwell, Holdaway & Uson, 1993; Holdaway, 1998). Ekers and Rots (1979) showed that mosaic observations extend the sampled spatial frequencies in a region around each (u,v) point sampled by the interferometer array, but a homogeneous array still depends heavily on single dish observations to sample spatial frequencies less than the antenna diameter, and the image fidelity is limited by pointing, and primary beam errors (Cornwell, Holdaway & Uson, 1993).

The CARMA telescope is a heterogeneous array of 10.4, 6.1 and 3.5 m antennas, with antenna configurations providing spacings from $\sim$ 4 m to 2 km. This heterogeneous array is well suited to imaging a wide range of spatial scales. The different antenna diameters allow a larger range of spatial frequencies to be sampled by interferometer observations, and the different primary beam patterns decouple the source brightness distribution from the primary beam illumination. There is still a central hole in the *uv* sampling, but the hole

is smaller which means that there is less information which needs complementary single dish observations. If we use the 10.4 m antennas to obtain the single dish observations, there is a large region of overlap in spatial frequencies which can be used to cross calibrate the single dish and interferometer observations. The heterogeneous interferometer observations by themselves provide an excellent cross calibration of the 3.5, 6.1 and 10.4 m antennas.

The 3.5 m antennas will first be used as a compact sub-array for SZ observations. In CARMA memo 25 we showed that good *uv* coverage can be obtained by locating the SZA array $\sim$ 30m south of the CARMA array center. Cross correlations between the CARMA and SZA arrays produce *uv* tracks which nicely fill the *uv* plane in the CARMA E configuration. The brightness sensitivity is not much changed because the eight 3.5 m antennas do not add much collecting area. However, the sensitivity to large scale structures is improved by sampling shorter *uv* spacings, and the density of *uv* samples is more than doubled which improves the image fidelity.

In BIMA memo 73, we simulated imaging with an array of 6.1 and 10.4 m antennas for three representative models: eight point sources, Cas A, and an eye chart. In all three models, the image fidelity improved as the *uv* sampling density was increased. We compared the images obtained with homogeneous and heterogeneous arrays. The heterogeneous array allows shorter *uv* spacings to be sampled directly using a compact configuration of the smaller antennas. This reliably recovered more of the total flux density and the corresponding large scale structure. The heterogeneous CARMA array produced better image fidelity than a homogeneous array with the same number of antennas and collecting area. By historical accident, the CARMA array has about the right ratio of antenna sizes to produce good image fidelity for mosaics.

The Cas A model and the eye charts are extended, complex sources with a similar distribution of spatial scales from $0.5''$ to a few arcmin, and give similar results. Cas A provides a real astronomical source brightness distribution, but it is easier to see the image defects on an easily recognized image like an eye chart.

In this memo, we simulate mosaic images of Saturn with the 23-antenna CARMA telescope in three compact configurations. Saturn provides an astronomical source model with an easily recognized structure. We use these simulations to analyze two separate problems. i) sampling the short spatial frequencies, ii) Nyquist sampling the large scale structure.

2. CARMA-23 Simulations

The simulations make model *uv* data sampled by the 23-antenna heterogeneous array using a model image of Saturn. The ring structure is $\sim 45''$ diameter, and we require $\sim 1''$ resolution to separate the rings. We simulated observations at 230 GHz with the CARMA array in the E, D and C configurations together with the cross correlations between the SZA and CARMA arrays. We will call these 23-antenna configurations the EZ, DZ and CZ configurations.

2.1. Data Sampling

The source brightness distribution is illuminated by the antenna reception pattern for each pair of antennas. The effective primary beam is the product of the voltage pattern of one antenna and the complex conjugate of the other. In order to image an extended source we need to correct the data for this illumination pattern.

In CARMA memo 5, we argue that errors in the voltage beam pattern of the larger antennas which lie within the main lobe of the voltage beam pattern of the smaller antennas will corrupt mosaic images. If we can measure the primary beam patterns well enough, then including 10.4 versus 3.5 m correlations provides additional *uv* data and primary beams to deconvolve the synthesized and primary beam responses from the image. If we can not determine the primary beam patterns well enough, the errors will degrade the image fidelity. Similarly, if the pointing centers of the antennas are offset, there will be large uncertainties in the resulting product of voltage patterns, and the asymmetric primary beam patterns rotate on the sky. For mosaic observations we would need to calculate a primary beam for each pointing, baseline, and integration. Whilst this is possible in principal, the increased computing burden is substantial, and the errors in the visibility data are hard to measure.

In order to keep the number and parameterization of the primary beam models manageable, the most convenient way to make mosaicing observations is to use the same pointing pattern for all antennas at the sample interval required for the largest antenna in the sub-array being used. In view of the discussion above, this mode is also likely to produce the best image fidelity in practice.

Sampling rates are set by both the largest and smallest antenna diameter. The Nyquist sample interval for the *uv* data, $\delta uv = D_{min}/2\lambda$. The Nyquist sample interval for the pointings, $\delta\theta = \lambda/2D_{max}$. The *uv* data for each pointing are oversampled by the larger antennas, and the pointing is oversampled by the smaller antennas. There is no loss in sensitivity since the oversampled data are properly accounted for in the imaging algorithms. Using the larger antennas on the longest interferometer baselines provides a more uniform sensitivity in the *uv* data and reduces the required *uv* data sample rate.

The 23-antenna heterogeneous array can thus be considered as a set of sub-arrays with a primary beam pattern for each pair of antenna diameters. Mosaic observations with the 23-antenna telescope (CARMA-23) produce 6 primary beam patterns for each pointing center; the products of the voltage patterns in cross correlations between the 3 antenna sizes. The different primary beam patterns illuminate the source structure providing independent information about the source brightness at each pointing center. The primary beam pattern depends on the aperture illumination and pointing of the antennas. In practice the mosaicing algorithms usually clip the primary beam model at the $\sim 5\%$ level, thus avoiding the uncertainties and variations in the primary beam response at low levels. Within the 5% level, the primary beam patterns are well approximated by Gaussian beam patterns. Table 1 lists the equivalent antenna diameter, primary beam FWHM and Nyquist sample interval at 230 GHz. Note that the 10.4 - 3.5 m correlations have almost the same effective primary beam pattern as the 6.1 m antennas, providing a method to measure and cross calibrate the primary beam patterns by comparing images from each sub-array.

3. Mosaicing Simulations

We made mosaicing simulations for three compact configurations of the 23-antenna array using the model image of Saturn described by Dunn etal (2004). *uv* data were created for each pointing center and primary beam pattern. Thermal noise, calculated using a double sideband receiver temperature 80 K and an atmospheric model with zenith opacity 0.26 at 230 GHz, was added to the *uv* data. We used a bandwidth 4 GHz and the antenna gains listed in Table 1. The *uv* data were sampled from -2 to +2 hours around transit which gives good azimuthal *uv* coverage for the CARMA antenna configurations, and minimizes antenna shadowing (see CARMA memo 5).

We used a hexagonal pointing pattern with $15''$ spacing. The $\sim 45''$ diameter source lies within the primary beam of the 6.1 and 3.5 m antennas and mosaic observations are not strictly required for these cross correlations. However, we wish to cross correlate these antennas with the 10.4 m antennas using the same pointing pattern for all antennas. The 3.5 m antennas effectively sample a guard band around the source brightness distribution, which helps the mosaicing algorithms to define the extent of the source. The resulting thermal noise in the image for each sub-array and pointing center is listed in Table 1.

The *uv* data were Fourier transformed to make images and deconvolved using Maximum Entropy (MEM) algorithms. The original image model was convolved to the same resolution by a Gaussian restoring beam and subtracted from the deconvolved image.

4. Results

Three different MEM deconvolutions were used: i) Using the interferometer data only with a total flux constraint. Single dish data were not included. ii) Using the single dish data as a default image. In this case, spatial frequencies obtained from the interferometer data replace those from the single dish data. iii) Joint deconvolution of the interferometer and single dish data. In this case, the extent to which the single dish data can be deconvolved is limited by our characterization of the primary beam and pointing errors in the single dish data. These three deconvolutions are compared in the three entries for each configuration in Table 2. The residual imaging errors are characterized by the total recovered flux, peak flux density and the RMS residuals. The image fidelity is listed in the last column as the ratio of the peak flux density to the on-source RMS in the residual image. The RMS was evaluated in a $50''$ bounding box.

The best image fidelity was obtained using the joint deconvolution of the interferometer and single dish data. The extent to which the single dish data can be deconvolved is limited by primary beam and pointing errors in the single dish data, as well as thermal noise and systematic residual errors such as ground pickup or atmospheric fluctuations.

For the single dish data, we used the 10.4 m antennas, and set the noise level at 1% of the peak flux density, since we want the noise estimate for the single dish data to include primary beam and pointing errors. More than one 10.4 m antenna can, and should, be used to reduce random and systematic noise from pointing, primary beam and atmospheric fluctuations, but the data are treated here as one antenna with a 1%

noise.

Using the single dish data as a default image, provides both a total flux estimate and low spatial frequencies unsampled by the interferometric mosaic. This gives higher image fidelity than just using the interferometer data with a total flux estimate.

Giving higher weight to the single dish data, as in the joint deconvolution, improves the image fidelity, but a 1% error may be unrealistic. In practice, primary beam and pointing errors will limit the image fidelity (Cornwell, Holdaway & Uson, 1993), but it is useful to compare the performance of the CARMA array without this limitation.

The EZ configuration gives the best image fidelity, but does not have sufficient resolution to separate the ring structure of Saturn at 230 GHz. Figure 1 shows the joint deconvolution for the DZ configuration. The DZ configuration provides a well sampled *uv* coverage and a very clean deconvolution with little of the flux density scattered out of the model image by poor *uv* sampling. The CZ configuration has better than $1''$ resolution, but the *uv* sampling is inadequate, and flux density is scattered out of the planet model image. Figure 2 shows the joint deconvolution including all the cross correlations between the CARMA and SZA arrays, but omitting the short spacings between 3.5 and 6.1 m which are sampled by the compact SZA array. Including these short spacings improves the image fidelity (Figure 3), but there is still considerable flux density scattered out of the model image.

Combining the DZ and CZ observations provides sufficient resolution and *uv* sampling to produce a nice image with good separation of the ring structure. Figure 4 shows the MEM deconvolution using the single dish to estimate the total flux density. Again we omitted the short spacings between 3.5 and 6.1 m. Better image fidelity is obtained with the joint deconvolution (Figure 5). The joint deconvolution provides better constraints on the large scale structure. Less flux is scattered out of the image model, the background sky is darker in Figure 5 than in Figure 4, and the image fidelity is higher. Figure 6 shows the joint deconvolution including the short spacings between 3.5 and 6.1 m leading to a further improvement in image fidelity.

These deconvolutions could be improved by tuning the parameters (noise level estimates, bounding box, subtracting an *a-priori* planet model, etc), but we wish to compare the different deconvolutions and configurations in a uniform way. In practice, the imaging errors will be dominated by noise and systematic errors in the *uv* data and deconvolution errors at these levels will not be significant for many sources.

5. Comparisons in the Image domain

In figures 1 to 6, the image has been convolved by a Gaussian restoring beam with FWHM fitted to the synthesized beam. This standard practice smooths over imperfections in the images at high spatial frequencies, which are less well sampled, and produces a more realistic source distribution, and with better brightness sensitivity (Jy/beam). Higher spatial frequencies are sampled in the *uv* data, and can be used in fitting model image parameters to the *uv* data.

In figures 7 to 10 we plot the MEM images, before convolution by the restoring beam to see the effects of the missing short spacings and *uv* sampling density, and to see the limitations of fitting model image parameters to the *uv* data. The CZ and CDZ configurations (Figures 7 and 8) have the same *uv* sampling at the highest and lowest spatial frequencies, so the limiting resolution is the same. The CDZ configuration has a higher *uv* sampling density at spatial frequencies sampled by the DZ configuration, which improves the definition of the ring structures. Both images omit spacings between 3.5 and 6.1 m. Figures 9 and 10 show the joint deconvolutions for the CZ and CDZ configurations including the interferometer spacings between 3.5 and 6.1 m. The image fidelity is further improved because the interferometer observations provide better data for these short spatial frequencies, than we could obtain from the joint deconvolution with the 10.4 m single dish data.

6. Comparisons in the Fourier domain

To see the effects of the *uv* sampling, we also compare the images in the Fourier domain. A radial distribution of the Fourier transform for the deconvolved and residual images shows most of the germane points for this almost circular source model (Figure 11). The solid black line shows the Saturn model. The amplitude shows a characteristic Bessel function response from the disk and ring system, but the power law distribution is otherwise remarkably similar to that for Cas A and eye chart models.

The red dashed line plots the Fourier transform of the MEM image, before convolving by a restoring beam. The radial distribution is plotted over the range of *uv* spacings sampled by the CDZ configuration, and follows the model structure quite well except at the highest spatial frequencies which are not well sampled at all azimuth angles in the (u,v) plane. The break away from the input model occurs at the largest *uv* distance which has good azimuthal sampling.

The lower two curves show the difference images between the MEM images and the original model image both convolved by the restoring beam. The image fidelity at different spatial frequencies is measured by the vertical distance from the model image. Both CZ and CDZ images include the spacings between 3.5 and 6.1 m and at low spatial frequencies the image fidelity is the same. The image fidelity is improved for the CDZ configuration at higher spatial frequencies by the higher density of *uv* samples.

7. Discussion

7.1. Short spacings and Single Dish Observations

The best image fidelity was obtained using a joint deconvolution of the interferometer and single dish data. The relative weight of these data in the deconvolution is determined from the theoretical RMS noise of the input interferometer and single dish images The mosaicing algorithm (MIRIAD's MOSMEM) attempts to reduce the residuals to have the same RMS as these. For a mosaic, the theoretical noise is position dependent, and is determined from information saved by INVERT. For the single dish image, the RMS noise

is assumed to be constant across the field, and was set at 1% of the peak flux density, since we want the noise estimate for the single dish data to include primary beam, pointing errors, spillover etc. This may be optimistic, especially for continuum observations, but the errors can be reduced by using more than one 10.4 m antenna for the single dish observations. Using the interferometer spacings between 3.5 and 6.1 m sampled by the 3.5 m antennas improves the image fidelity because the interferometer observations provide better quality data for these short spatial frequencies, than can be obtained from the joint deconvolution with the 10.4 m single dish data. Ekers and Rots (1979) showed that mosaic observations extend the sampled spatial frequencies in a region within the antenna diameter around each (u,v) point sampled by the interferometer array (see e.g. Holdaway, 1998). The heterogeneous array provides more collecting area at the shortest spacings from adjacent small and large diameter antennas. In practice the mosaicing algorithms appear to extend the sampled spatial frequencies to about 1/2 to 2/3 of the antenna diameter. In a direct test of the Ekers & Rots algorithm (BIMA memo 45), we used a Fourier transform of the mosaic data w.r.t. the pointing center (MIRIAD's UVPNT task) to generate more dense sampling of *uv* data. The mosaic data does indeed extend the *uv* sampling, but the image fidelity is not high. For the small mosaics we have used, a direct interferometer observation gives a higher quality measurement than a spatial frequency derived from the mosaic. We still depend on the single dish data for spatial frequencies between zero and the shortest interferometer spacing.

7.2. Density of *uv* Sampling

Figure 11 clearly shows the improvement in image fidelity of the Saturn image at higher spatial frequencies which results from higher density of *uv* samples obtained by combining CZ and DZ configurations. This is consistent with our earlier simulations in BIMA memo 73, where we used 3 different source models: eight point sources, Cas A, and an eye chart. In all these models, the image fidelity improves as the *uv* sampling density is increased, as expected in theory. Sampling short spacings does not solve all our problems; we also need to sample the larger spatial frequencies at the Nyquist interval to obtain the best image fidelity. In some cases, this missing data can be provided from an *a-priori* model, e.g. by subtracting a disk in the case of planet observations, but for other, unknown, extended source distributions, unsampled spatial frequencies are missing information, and will degrade the image fidelity.

8. Conclusion

The heterogeneous 23-antenna CARMA telescope provides some interesting advantages compared with homogeneous arrays:

1. The different antenna diameters allow a larger range of spatial frequencies to be sampled by interferometer observations.

2. The different primary beam patterns decouple the source brightness distribution from the primary beam illumination.

3. The central hole in the *uv* sampling is smaller which means that there is less information which depends on single dish observations.

4. There is a large region of overlap in spatial frequencies which can be used to cross calibrate the single dish and interferometer observations.

5. The heterogeneous interferometer observations provide excellent cross calibration of the 3.5, 6.1 and 10.4 m antennas.

6. The 3.5 m antennas effectively sample a guard band around the source brightness distribution, which helps the mosaicing algorithms to define the extent of the source. These observations of a guard band without having to make observations at extra pointing centers is an unexpected bonus.

9. References

D. E. Dunn, I. de Pater, M. Wright, M. Hogerheijde and L. A. Molnar, July 2004, *High Quality BIMA/OVRO Images of Saturn and its Rings at 1.3 and 3.0 mm*, AJ submitted.

BIMA memo 45, *BIMA Array response to extended structure*, M.C.H. Wright, 1999, http://bima.astro.umd.edu/memo

BIMA memo 73, *Image Fidelity*, M.C.H. Wright, 1999, http://bima.astro.umd.edu/memo/memo.html

Sault, R.J., Staveley-Smith, L & Brouw, W.N., 1996, *An approach to interferometric mosaicing*, A&A Supp., 120, 375

Bob Sault & Neil Killeen, 1999, *Miriad Users Guide*, http://www.atnf.csiro.au/computing/software/miriad

Holdaway. M.A., 1999, *Mosaicing with Interferometer Arrays*, ASP Conference series 180, 401.

Cornwell, T.J., Holdaway, M.A. & Uson, J.M., 1993, *Radio-interferometric imaging of very large objects: implications for array design*, A&A 271, 697.

CARMA memo 5, *Compact Configuration Evaluation for CARMA*, Melvyn Wright, Sep 2002.

CARMA memo 19, *Version 1 CARMA Configurations for Cedar Flat*, Tamera Helfer and Melvyn Wright, February 2004.

CARMA memo 20, *Version 2 CARMA Configurations for Cedar Flat*, Tamera Helfer, February 2004.

CARMA memo 25, *SZA location at CARMA site*, Melvyn Wright, June 2004.

Ekers, R. D., & Rots, A.H. 1979, in IAU Col. 49, *Image Formation from Coherence Functions in Astronomy* , ed. van Schooneveld, C. (Dordrecht:Reidel), p.61

Holdaway, M. A., 1998, *Mosaicing with Interferometer Arrays*, in Synthesis Imaging in Radio Astronomy II, ASP Conference Series, G. B. Taylor, C. L. Carilli and R. A. Perley (eds)

Table 1: CARMA-23 at 230 GHz

Antennas	Equivalent diameter	FWHM	Nyquist interval	Gain	Thermal noise
m x m	m	arcsec	arcsec	Jy/K	mJy
10.4 x 10.4	10.4	28	12.5	43	0.76
10.4 x 6.1	8.0	36		73	0.69
6.1 x 6.1	6.1	47	21.3	126	1.4
10.4 x 3.5	6.0	48		128	1.7
6.1 x 3.5	4.6	63		220	2.4
3.5 x 3.5	3.5	83	37.1	383	9.5

Table 2: Mosaicing Simulations for Saturn at 230 GHz. Each configuration lists 3 simulations: i) MEM deconvolution with total flux constraint, ii) using single dish as a default image, iii) joint deconvolution of interferometer and single dish data. The CZ and CDZ configurations list: i) omitting and ii) including interferometer spacings between 3.5 and 6.1 m.

Config	Beam	Model Flux	Peak	Image Flux	Peak	Residual: Rms	Max	Min	Fidelity
EZ	4.59 x 3.83	1160	72.24	1208.50	71.87	0.25	0.67	-0.84	284
EZ	4.59 x 3.83	1160	72.24	1210.78	71.91	0.25	0.69	-0.83	282
EZ	4.59 x 3.83	1160	72.24	1184.44	71.59	0.18	0.54	-0.62	398
DZ	2.12 x 1.91	1160	16.78	1441.87	17.16	0.91	0.84	-3.15	19
DZ	2.12 x 1.91	1160	16.78	1455.42	17.40	0.52	0.75	-1.70	33
DZ	2.12 x 1.91	1160	16.78	1198.77	16.67	0.33	0.38	-1.26	49
CZ	0.87 x 0.76	1160	2.74	1557.89	2.49	0.21	0.54	-0.54	12
CZ	0.87 x 0.76	1160	2.74	1440.47	2.58	0.15	0.42	-0.43	17
CZ	0.87 x 0.76	1160	2.74	1201.81	2.95	0.09	0.28	-0.37	30
CZ	0.87 x 0.76	1160	2.74	1347.15	2.98	0.06	0.16	-0.32	45
CZ	0.87 x 0.76	1160	2.74	1328.08	2.93	0.05	0.17	-0.31	51
CZ	0.87 x 0.76	1160	2.74	1161.08	2.91	0.06	0.22	-0.26	49
CDZ	1.41 x 1.26	1160	7.37	1469.16	7.57	0.08	0.30	-0.19	87
CDZ	1.41 x 1.26	1160	7.37	1471.85	7.68	0.08	0.29	-0.24	87
CDZ	1.41 x 1.26	1160	7.37	1197.83	7.35	0.05	0.18	-0.22	125
CDZ	1.41 x 1.26	1160	7.37	1283.39	7.55	0.04	0.14	-0.18	189
CDZ	1.41 x 1.26	1160	7.37	1283.18	7.57	0.03	0.12	-0.14	229
CDZ	1.41 x 1.26	1160	7.37	1175.16	7.46	0.03	0.09	-0.13	249

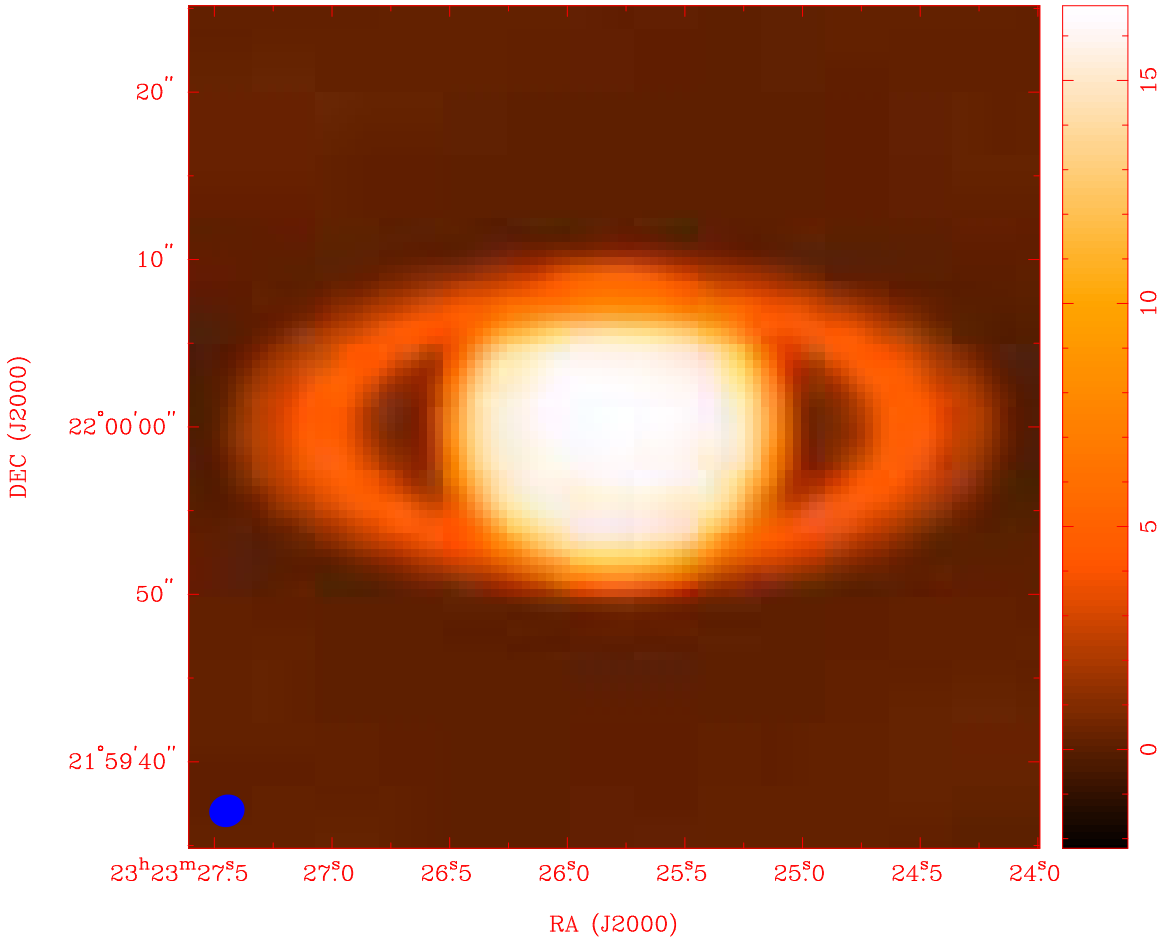

Fig. 1.— Joint deconvolution image using CARMA DZ configuration. Gaussian beam FWHM 2.12 x 1.91 arcsec, shown in lower left corner

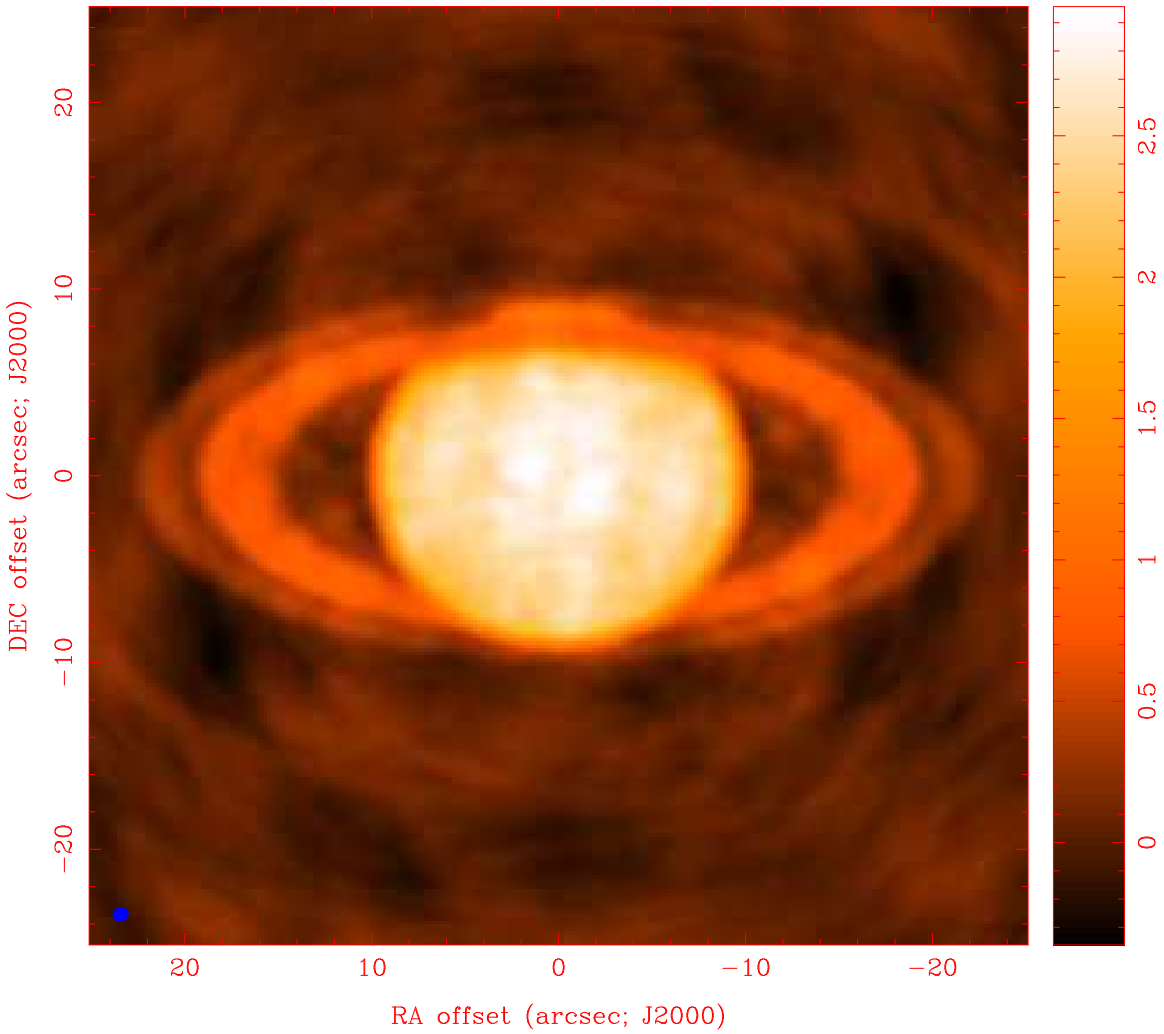

Fig. 2.— Joint deconvolution image using the CARMA CZ configuration, including all the cross correlations between the CARMA and SZA arrays, but omitting the short spacings between 3.5 and 6.1 m which are sampled by the compact SZA array. Gaussian beam FWHM 0.87 x 0.76 arcsec, shown in lower left corner

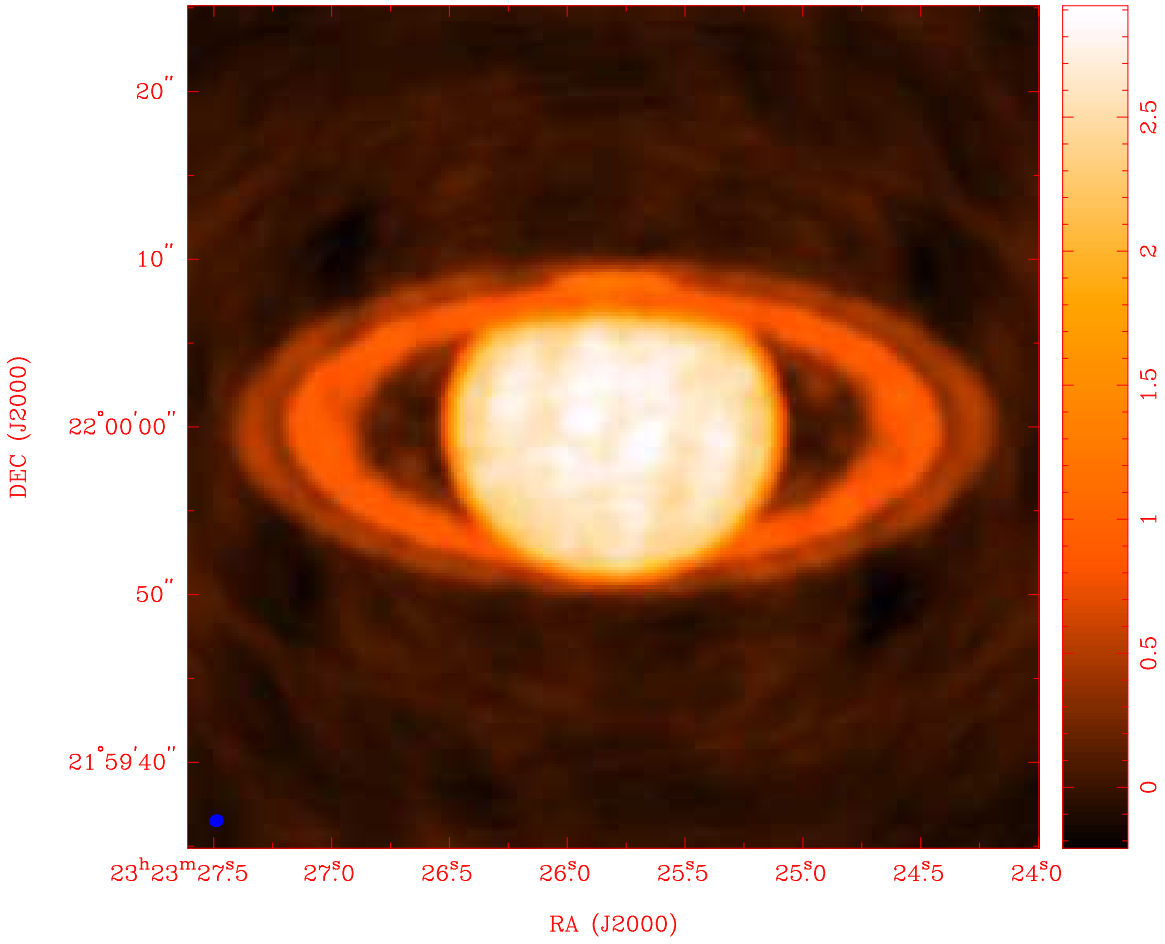

Fig. 3.— Joint deconvolution image using the CARMA CZ configuration including the short spacings between 3.5 and 6.1 m. Gaussian beam FWHM 0.87 x 0.76 arcsec, shown in lower left corner

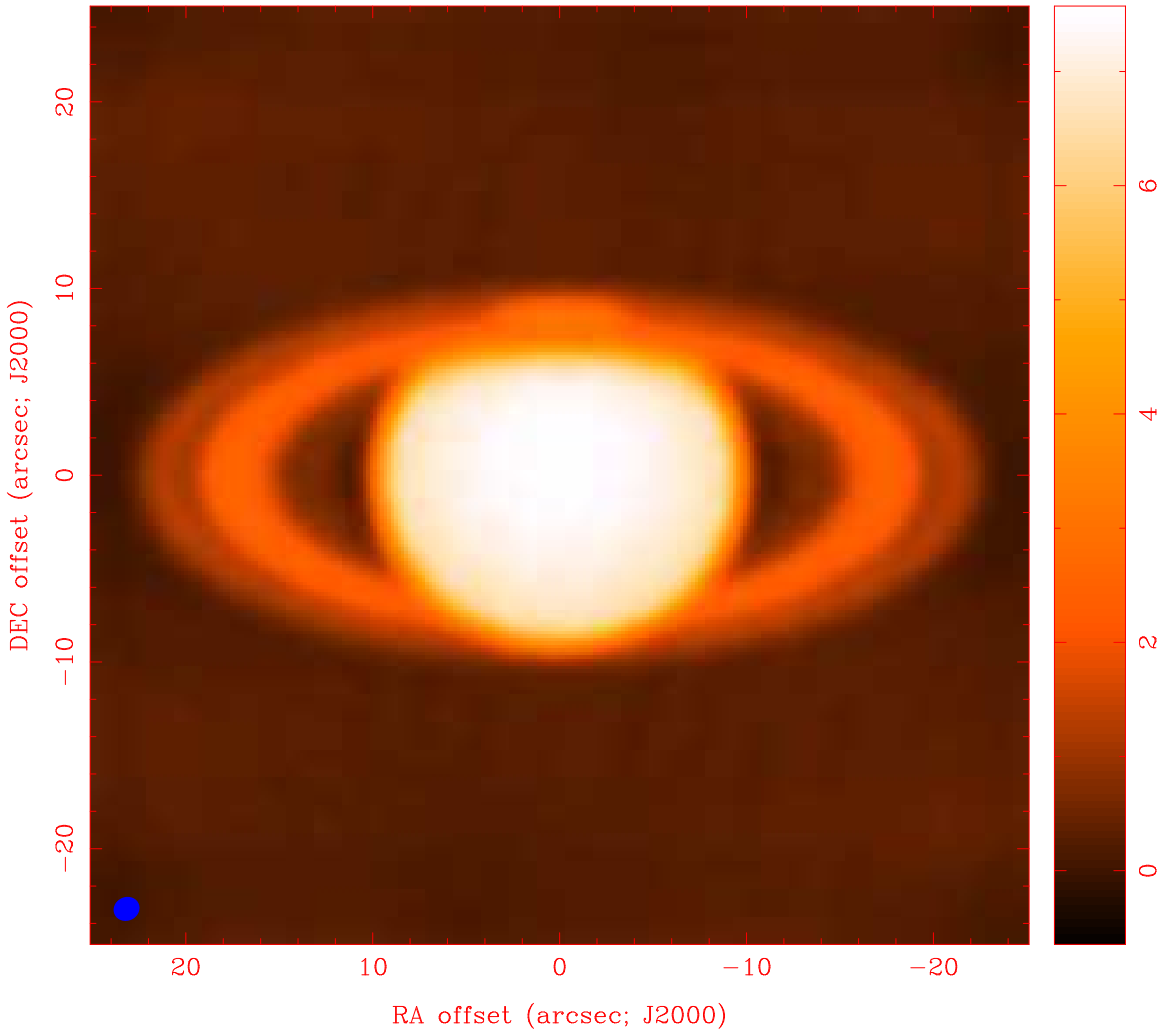

Fig. 4.— MEM deconvolution using the single dish to estimate the total flux density. CARMA CZ + DZ configurations, including all the cross correlations between the CARMA and SZA arrays, but omitting the short spacings between 3.5 and 6.1 m which are sampled by the compact SZA array. Gaussian beam FWHM 1.41 x 1.26 arcsec, shown in lower left corner.

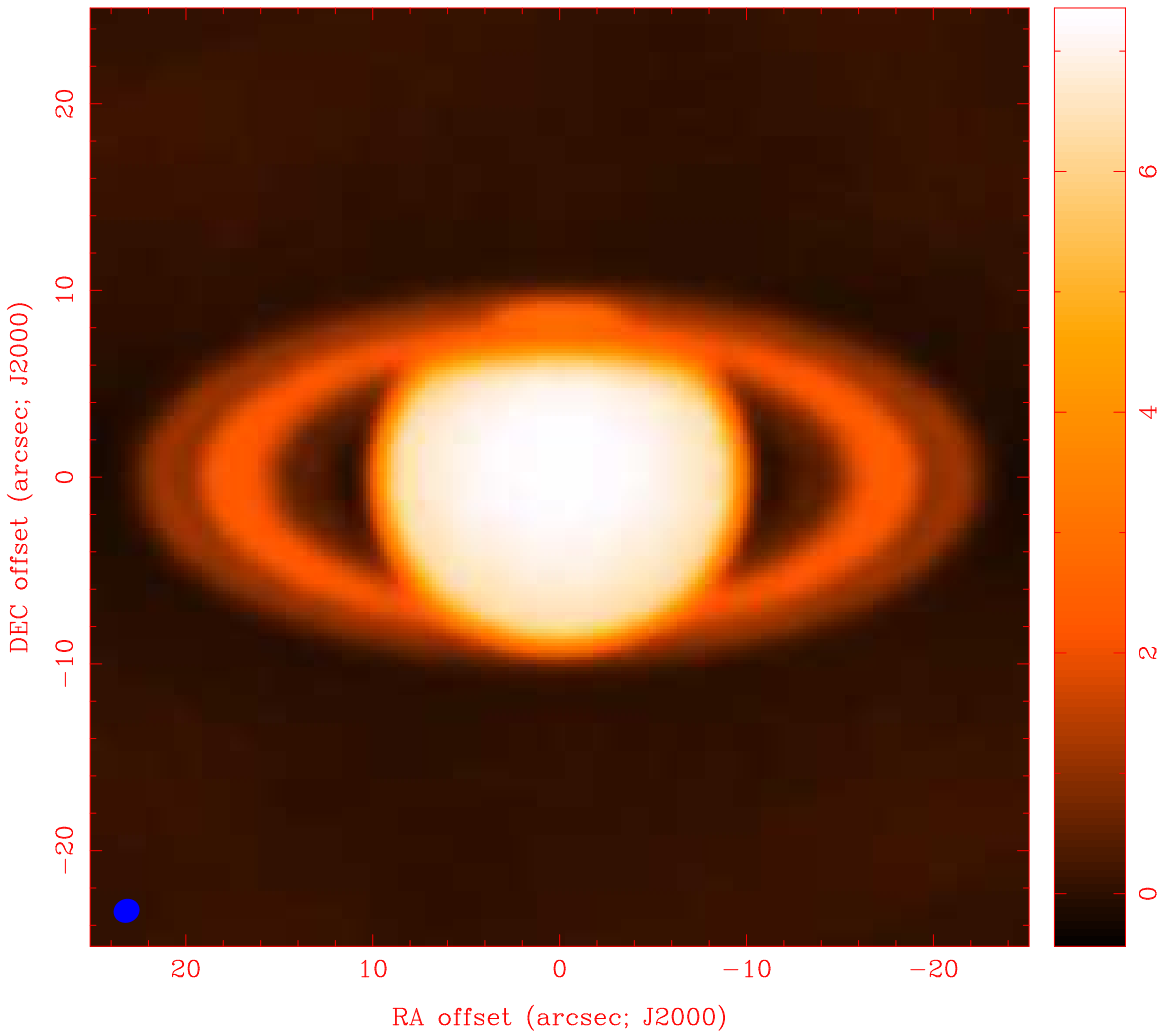

Fig. 5.— Joint deconvolution image using CARMA CZ + DZ configurations including all the cross correlations between the CARMA and SZA arrays, but omitting the short spacings between 3.5 and 6.1 m which are sampled by the compact SZA array. Gaussian beam FWHM 1.41 x 1.26 arcsec, shown in lower left corner.

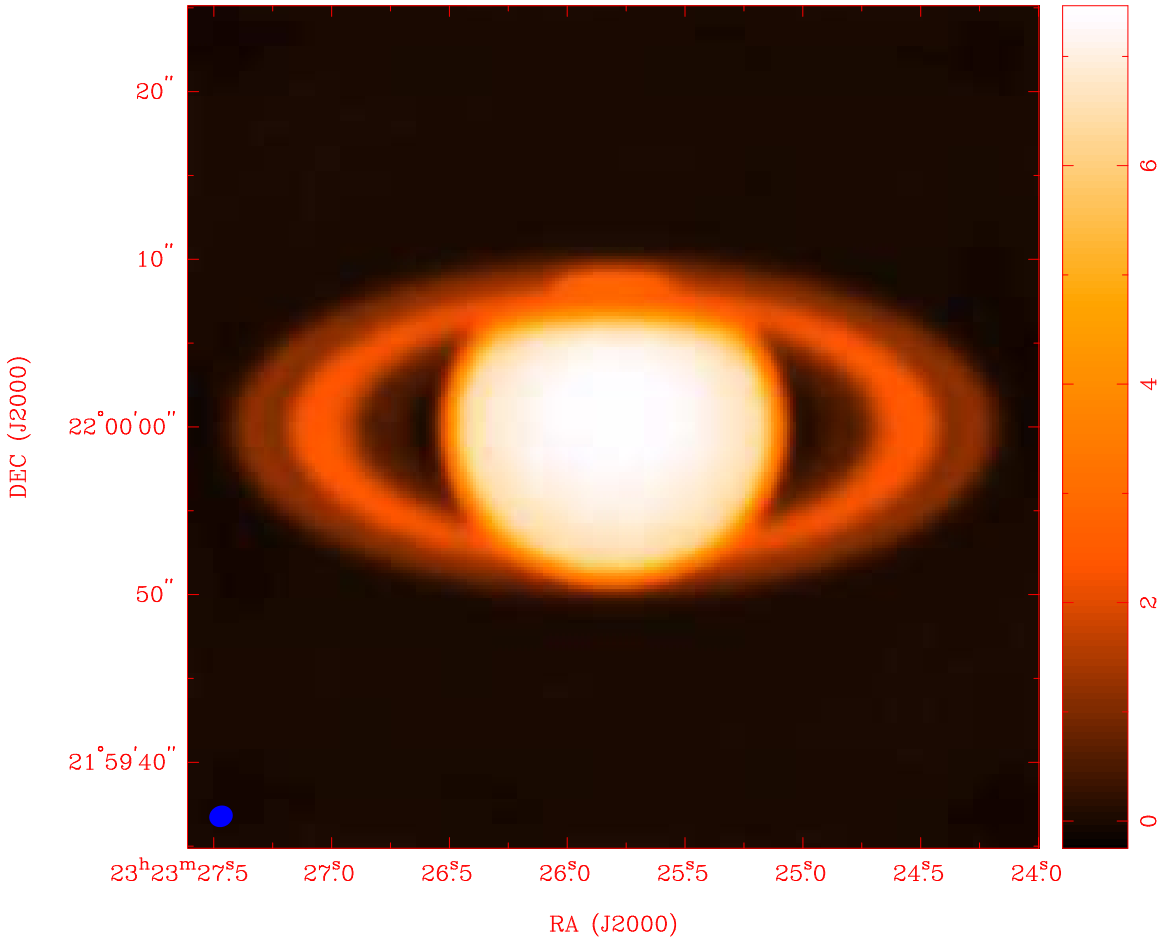

Fig. 6.— Joint deconvolution image using CARMA CZ + DZ configurations including the short spacings between 3.5 and 6.1 m. Gaussian beam FWHM 1.41 x 1.26 arcsec, shown in lower left corner.

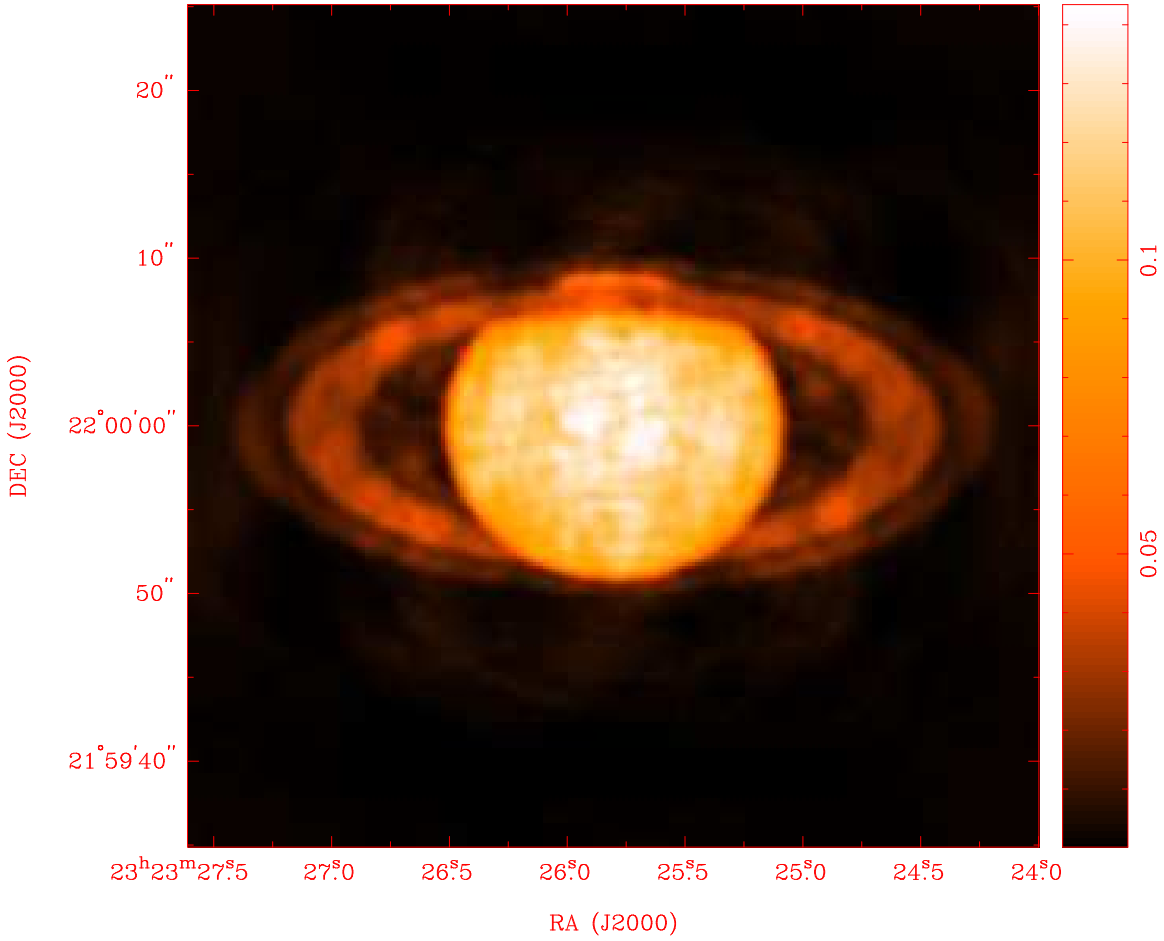

Fig. 7.— MEM joint deconvolution image using CARMA CZ configuration, including all the cross correlations between the CARMA and SZA arrays, but omitting the short spacings between 3.5 and 6.1 m which are sampled by the compact SZA array.

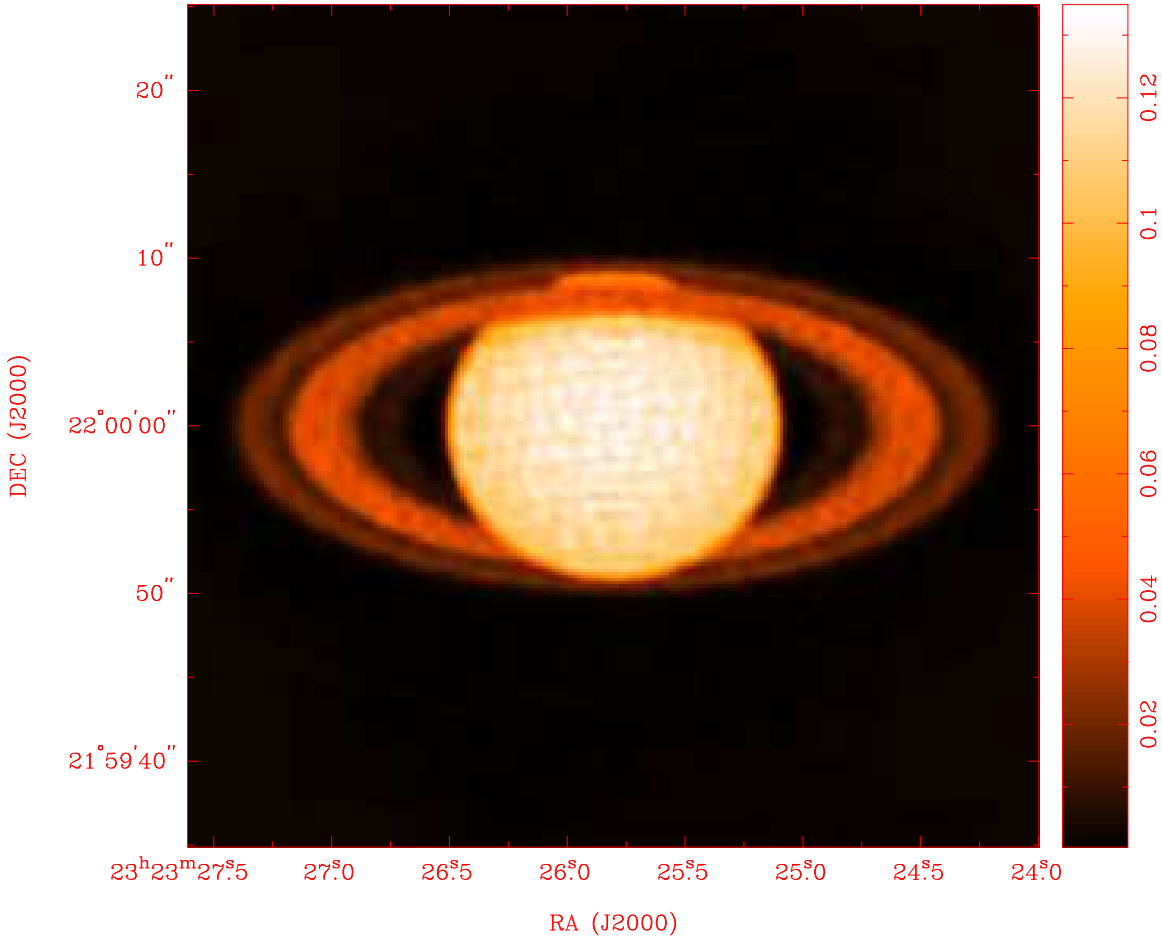

Fig. 8.— MEM joint deconvolution image using CARMA CZ + DZ configurations, including all the cross correlations between the CARMA and SZA arrays, but omitting the short spacings between 3.5 and 6.1 m which are sampled by the compact SZA array.

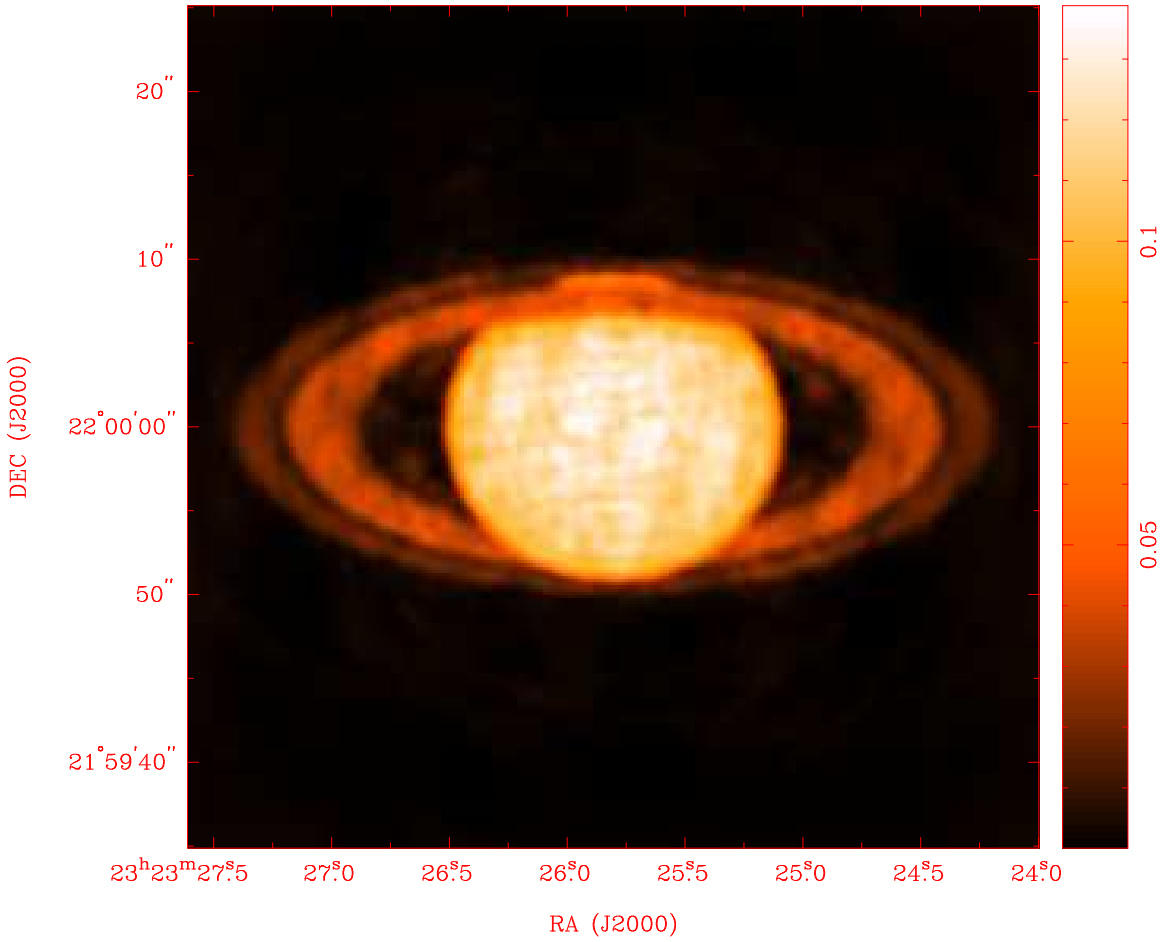

Fig. 9.— MEM joint deconvolution image using CARMA CZ configuration including the short spacings between 3.5 and 6.1 m.

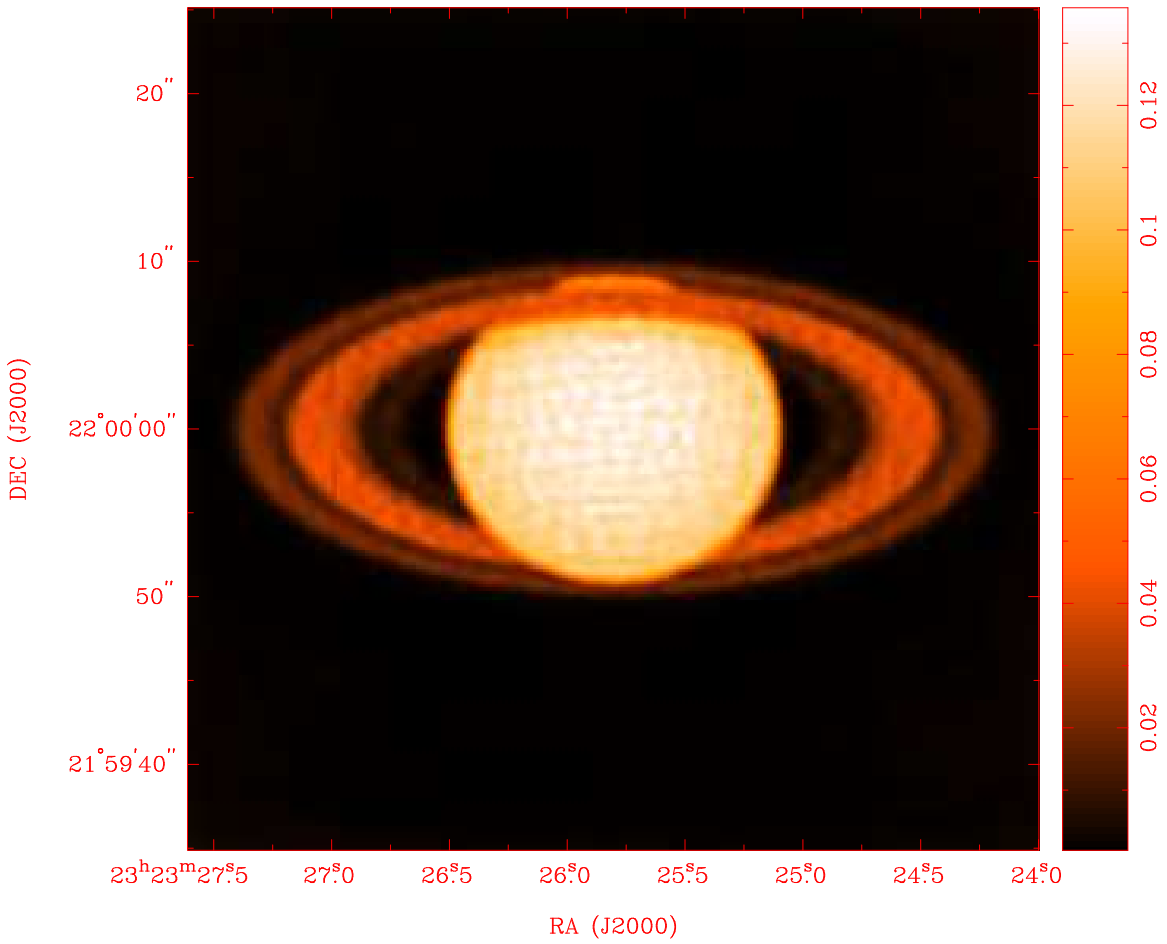

Fig. 10.— MEM joint deconvolution image using CARMA CZ + DZ configurations including the short spacings between 3.5 and 6.1 m.

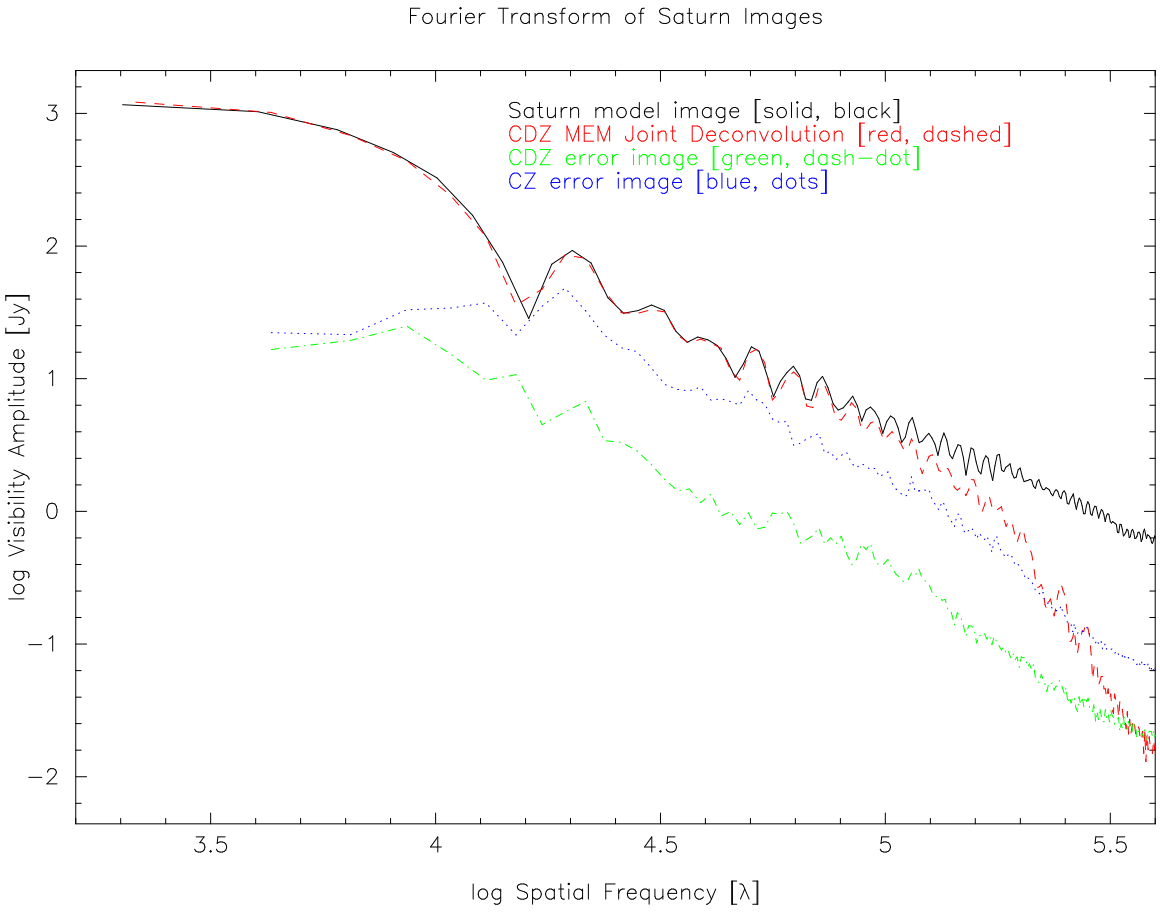

Fig. 11.— Radial distribution of the Fourier transform of Saturn Images. The solid black line shows the Saturn model. The amplitude shows a characteristic Bessel function from the disk and ring system. The red dashed line plots the Fourier transform of the MEM image, before convolving by a restoring beam. The radial distribution is plotted over the range of *uv* spacings sampled by the CDZ configuration. The lower two curves show the difference images between the MEM images and the original model image both convolved by the restoring beam.